Pressure-induced structural transitions triggering dimensional crossover in the lithium purple bronze $Li_{0.9}Mo_6O_{17}$

M. K. Tran,[1] A. Akrap,[1,2] J. Levallois,[1] J. Teyssier,[1] P. Schouwink,[1,3] C. Besnard,[1] P. Lerch,[4] J. W. Allen,[5]
M. Greenblatt,[6] and D. van der Marel[1,*]

[1] *Département de Physique de la Matière Quantique, Université de Genève, Quai Ernest-Ansermet 24, CH-1211 Genève 4, Switzerland*
[2] *Département de Physique, Université de Fribourg, Chemin du Musée, CH-1700 Fribourg, Switzerland*
[3] *Institut des sciences et ingénierie chimiques, EPFL, Lausanne, Switzerland*
[4] *Infrared Beamline, Swiss Light Source, Paul Scherrer Institute, CH-5232 Villigen-PSI, Switzerland*
[5] *Randall Laboratory, University of Michigan, Ann Arbor, Michigan 48109, USA*
[6] *Department of Chemistry and Chemical Biology, Rutgers University, 123 Bevier Road, Piscataway, New Jersey 08854*

(Received 14 March 2021; revised 28 May 2021; accepted 2 June 2021; published 14 June 2021)

At ambient pressure, lithium molybdenum purple bronze ($Li_{0.9}Mo_6O_{17}$) is a quasi-one-dimensional solid in which the anisotropic crystal structure and the linear dispersion of the underlying bands produced by electronic correlations possibly bring about a rare experimental realization of Tomomaga-Luttinger liquid physics. It is also the sole member of the broader purple molybdenum bronzes family where a Peierls instability has not been identified at low temperatures. The present paper reports a pressure-induced series of phase transitions between 0 and 12 GPa. These transitions are strongly reflected in infrared spectroscopy, Raman spectroscopy, and x-ray diffraction. The most dramatic effect seen in optical conductivity is the metalization of the *c* axis, concomitant to the decrease in conductivity along the *b* axis. This indicates that high pressure drives the material away from its quasi-one-dimensional behavior at ambient pressure. Although the first pressure-induced structure of the series is resolved, the identification of the underlying mechanisms driving the dimensional change in the physics remains a challenge.

DOI: 10.1103/PhysRevB.103.235124

I. INTRODUCTION

The family of purple bronzes gives access to a broad array of ground states: among them superconductor, charge-density wave (CDW), spin-density wave, metal-insulator transition, or a possible realization of Tomonaga Luttinger liquid. The purple molybdenum bronze family $A(Mo_6O_{17})$, $A =$ Tl, Li, Na, and K was intensively investigated since the 1960s, and each of its members was found to be a charge-density wave material; the exception being the lithium molybdenum bronze [1]. This system provides a very interesting experimental playground to investigate the signature of strongly correlated one-dimensional physics, i.e., Tomonaga-Luttinger liquids, present, in particular, in the spectral function of angle-resolved photoemission spectroscopy studies [2,3].

The transport properties of $Li_{0.9}Mo_6O_{17}$ are very anisotropic [4,5] as three orders of magnitude stand between the most insulating axis (a) and the most conducting one (b). The b axis resistivity displays a metallic behavior down to ~25 K where a sharp upturn occurs which is eventually followed in some samples by a superconducting transition below 2 K. The most debated aspect of $Li_{0.9}Mo_6O_{17}$ is the cause of the 25-K resistivity upturn [6,7]. The low-dimensional behavior of the material and its Fermi surface prone to nesting have, from the early studies, suggested the opening of a CDW gap as the explanation for the resistivity upturn [4]. However, no evidence for a CDW has been reported using structural probes, such as x-ray and neutron diffraction, and recent observations of the charge state using Nuclear Magnetic Resonance show that the electric-field gradient and the distribution remain constant as a function of temperature, indicating the absence of a CDW [8,9].

$Li_{0.9}Mo_6O_{17}$ was initially classified as a quasi-two-dimensional material with strong transport anisotropy, but following the resolution of its crystal structure [12] it was considered as a quasi-one-dimensional material. The structure, shown in Fig. 1, is described by the monoclinic $P2_1/m$ space group. The main structural elements are MoO_6 octahedra organized in slabs consisting of four layers of octahedra terminated by MO_4 tetrahedra on either side. The Li ions (not shown in Fig. 1) are situated between the slabs. In this paper we will follow the convention used by Onada *et al.* [12] where the unique axis b and the c axis at right angles with b are both parallel to the slabs. The a axis has an angle $\beta = 90.61^\circ$ with c, and it is perpendicular to b. The lattice parameters are given in Table I. A different (but equally valid) axis labeling convention that interchanges a and c is used in much of the literature, especially papers reporting experimental results, so it is important to check which convention is used in any particular paper. A pair of octahedra, individually made out of one molybdenum atom surrounded by six oxygen atoms, forms two well-separated zigzag chains running along the b axis. The anisotropy in the transport properties identifies the b axis as the most conducting direction a as the most insulating one and the c axis in between these two (see, e.g., Ref. [5]

---

[*] dirk.vandermarel@unige.ch

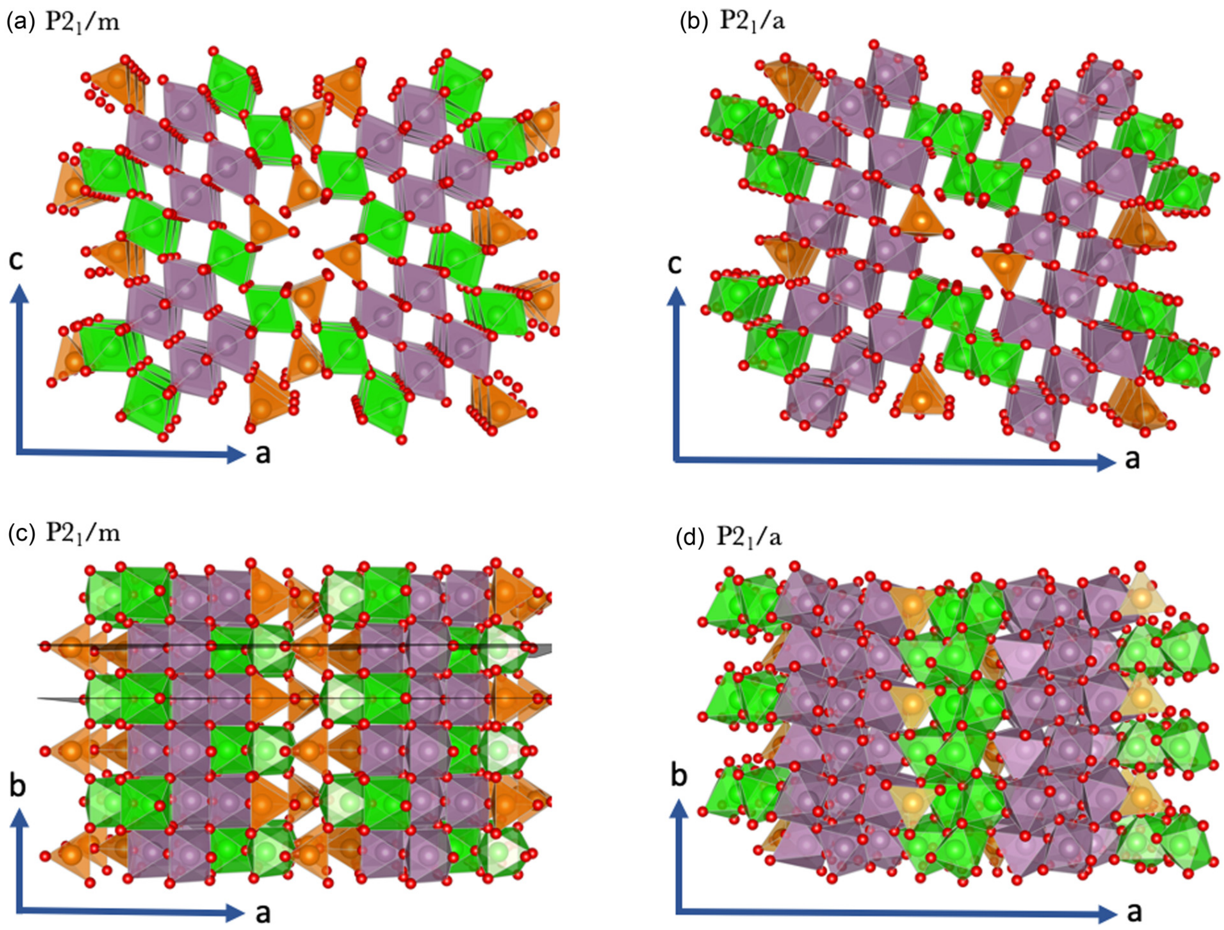

FIG. 1. Crystal structure at low pressure [panels (a) and (c)] and for pressure between 3.6 and 6 GPa [panels (b) and (d)]. To avoid clutter the Li atoms are not shown. The projection is along the b (c) axis for panels (a) and (b) [(c) and (d)]. The lattice parameters are given in Table I. The horizontal planes in panel (c) are mirror planes. This graph was generated with the open source program VESTA [10] using the structural parameters available in Ref. [11].

but pay attention to the reversed choice of the a and c axes) suggesting that conduction takes place primarily within the MoO_6 octahedra zigzag chains.

A recent theoretical study [7] employing the Nth-order muffin-tin orbital method has obtained an analytical representation of the six lowest-energy Mo t_{2g} bands, which are found to be essentially two dimensional (2D). Strong covalent bonding fully gaps four of these bands, leaving in the gap two nearly degenerate metallic chain bands crossing E_F to define the Fermi surface. The dispersion of these two chain bands is highly one dimensional, very strong along k_b, two orders of magnitude weaker along k_c, and essentially negligible along k_a (same axis definitions used as in the present paper), in good qualitative agreement with the observed resistivity anisotropy.

TABLE I. Space group and lattice parameters from x-ray diffraction for the different pressure ranges of the crystallographic phases of purple bronze. For the low-pressure phase (space-group $P2_1/m$) we adopt the convention used by Onada *et al.* [12] where b and c are parallel to the slabs. To facilitate comparison of the crystal axis of the different phases we use $P2_1/a$ for the high-pressure phase instead of the standard setting $P2_1/c$. $N_{fu/pc}$ represents the number of formula units per primitive cell, and V_{fu} represents the volume per formula unit. Between 3 and 3.6 GPa $P2_1/m$ and $P2_1/a$ are observed together. The last column indicates the experimental probe with which the phase was observed. XRD, IR, and R refer to x-ray diffraction, infrared spectroscopy, and Raman spectroscopy, respectively.

Space group	a Å	b Å	c Å	β Degrees	$N_{fu/pc}$	V_{fu} Å^3	Pressure Gpa	Probe
$P2_1/m$	12.451(9)	5.486(3)	9.347(7)	90.7(2)	2	319	0–3.6	XRD,IR,R
$P2_1/m$ and $P2_1/a$							3–3.6	XRD,IR,R
$P2_1/a$	23.587(8)	5.11(1)	9.495(6)	93.3(1)	4	285	3–6	XRD,IR,R
Unresolved	11.34(4)	4.94(3)	9.42(2)	97.4(2)	2	261	6–9	XRD,IR,R
							9–11	IR,R
							>11	R

The simplest model conceptualization is that of conducting chains with a weak interchain hopping parameter $t_\perp$ [13,14] as might be imagined from Fig. 1 or from the first figure of the work of Lu *et al.* [15] (but taking note of their reversed choice of *a* and *c* axes). However, in the detailed study of Ref. [7], the effective downfolded perpendicular couplings in $Li_{0.9}Mo_6O_{17}$ are found to be of much longer range and cannot be modeled in a simple tight-binding fashion due to a resonant energy dependence arising from mixing with the four gapped bands. These couplings lead to a splitting and a complex warping and shaping of the two-band Fermi surface in a way that is very sensitive to the value of E_F, i.e., to the stoichiometry of the sample.

Previous optical investigations have reported a very anisotropic response [16,17]. A detailed study of the infrared properties [17] showed free-carrier optical conductivity along the (most conducting) *b* axis on the order of 2 kS/cm—a value in line with bad metallicity of $Li_{0.9}Mo_6O_{17}$—and two orders of magnitude smaller conductivity in the direction perpendicular to *b* in the cleavage plane (the *c* axis, in the notation of the present paper). Moreover, for all temperatures the low-frequency response strongly differs from Drude behavior. In particular, the conductivity is almost frequency independent at low frequencies and exhibits a strong peak at 70 meV as well as smaller peaks at lower energy, whose intensities depend strongly on temperature [17]. The non-Drude response may be caused by low dimensionality in combination with charge-carrier localization, electron correlation, or dimensional crossover [18]. Electronic transport under pressure showed a stabilization of superconductivity at the expense of the resistivity upturn [19]. As the application of pressure generally tends to enhance the orbital overlaps in a low-dimensional solid, other ground states might be favored [20]. From the theoretical point of view, a crossover from a Luttinger liquid behavior to a 2D metallic behavior was proposed [18,21] for one-dimensional (1D) conducting chains with the introduction of a small coupling. Reports of such a crossover are supported by thermal expansion experiments [22].

In the present paper, we explore how applied pressure tunes the optical response of $Li_{0.9}Mo_6O_{17}$. This allows us to assess the involved changes in the electronic conduction channels. Our most important finding is that the marked anisotropy of ambient-pressure optical properties vanishes above 6 GPa, concomitant to a structural phase transition. Overall, $Li_{0.9}Mo_6O_{17}$ undergoes several phase transitions under pressure confirmed by our x-ray diffraction data, further enriching its complex phase diagram. In the high-pressure phase, this compound appears to be no longer a quasi-1D conductor.

II. RESULTS

We measured x-ray diffraction, Raman, and infrared spectra of $Li_{0.9}Mo_6O_{17}$ crystals as a function of pressure in the pressure ranges of 0–15 GPa (Raman and infrared) and 0–10 GPa (x rays). The crystal growth procedure used for the $Li_{0.9}Mo_6O_{17}$ crystals is described in Refs. [1,23].

X-ray diffraction. Single crystals of approximate dimensions $30 \times 40 \times 20$ μm were first characterized using home-based x-ray diffractometers. Subsequently, synchrotron x-ray diffraction was performed under pressure in diamond-anvil cells both on single crystals as well as a powder ground from the same sample batch. These measurements were performed in two successive sessions at the High-Pressure Beamline ID 27 and at the Swiss Norwegian Beamline BM 01 of the European Synchrotron Radiation Facility (ESRF). The high-pressure experiments at ID 27 were performed at a wavelength of 0.3738 Å, using BETSA-type membrane diamond-anvil cells (opening angle 68°) and He as a pressure medium. At BM 01, $\lambda = 0.68043$ Å, samples were loaded into ETH-type diamond-anvil cells [24,25] (opening angle 90°) and pressurized by manually tightening four screws, in an ethanol-methanol pressure medium, which has a hydrostatic pressure limit of ~10 and 11 GPa. In all experiments the samples, crystals, or powder were loaded into a 600-μm laser-drilled sample chamber, using preindented stainless-steel gaskets of ~80-μm thickness. Pressure was monitored in all cases with ruby spheres of ~3 μm using the ruby fluorescence line. The powder-diffraction experiment was used to detect phase transformations (see the Appendix) as well as to solve the general topology of the phase between 3 and 6 GPa (data used: 5.9 GPa). The evolution of normalized lattice parameters is shown in Fig. 2.

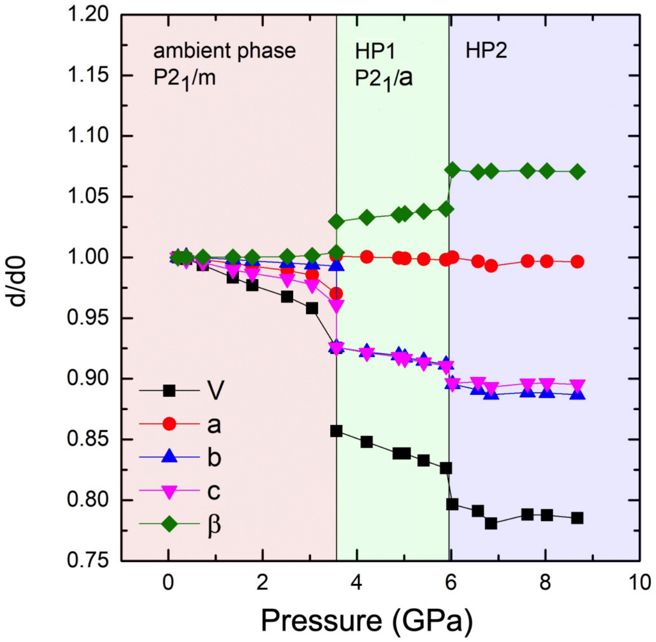

FIG. 2. Pressure dependence of the lattice parameters d ($d = a, b, c, \beta, V$) relative to the value at zero pressure (d_0), determined by Le Bail refinements using powder-diffraction data. For the high-pressure phase 2 (HP2) the space group could not be resolved.

Raman spectra were measured on the *bc* cleavage plane in backscattering geometry at room temperature as a function of pressure in the same pressure cell, using Daphne oil 7373 as a pressure transmitting medium and ruby chips as pressure sensors. The addition to a rotating half-wave plate allowed to disentangle the spectral contribution of XX and XY polarizations. It was, however, not possible to match the crystallographic *b* and *c* axes with the polarization of the laser

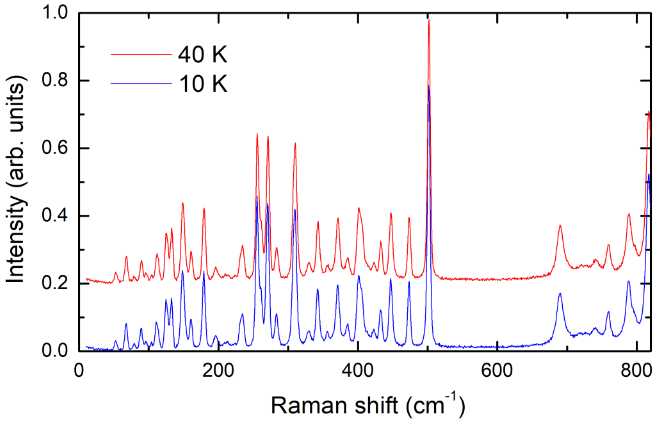

FIG. 3. Ambient-pressure unpolarized Raman spectra at 40 K (red curve) and 10 K (blue curve).

beam. The Raman spectra at ambient pressure are displayed in Fig. 3. The 10-K spectrum shows a large number of sharp phonon modes, consistent with a large unit cell and low symmetry of the compound. Panel (b) shows that the modes do not exhibit any noticeable changes with temperature, more specifically, when crossing the temperature of the upturn in the resistivity. Due to the fact that a CDW breaks the translational symmetry of the crystal, a transition into a CDW state would be accompanied by the appearance of additional Raman modes. The absence of additional modes below 25 K in the spectra of Fig. 3 is a strong indication that the resistivity upturn below 25 K is not caused by a CDW. The evolution with pressure of the Raman spectra obtained for (a) XX and (b) XY polarizations are presented in Figs. 4 and 5.

Optical spectroscopy. Ambient pressure infrared reflectance spectra were obtained by measuring the intensity reflected from the sample at ambient pressure and calibrated against a gold layer evaporated *in situ* on the sample surface (Fig. 6). Crystal surfaces were oriented parallel to the *bc* plane, and a rotating gold wire polarizer was used to isolate the *b*- and *c*-axis components of the reflectivity tensor. The ambient pressure reflectivity at room temperature is shown in Fig. 6 for the electric field polarized along the *b* and *c* axes, respectively. This result reproduces the previous spectra determined by Choi *et al.* [17]. A strong anisotropy is evident from the reflectivity data where the *b* axis is metallic and the *c* axis is insulating. The *b* axis shows reflectivity that tends to unity as photon energy decreases, consistent with a metallic response. A broad shoulder from 300 to 500 meV may be linked to the screened plasma edge. In contrast, the *c* axis shows sharp phonon features that dominate the low-energy reflectivity. The overall low-energy value of the reflectivity is significantly smaller than along the *b* axis, pointing to an insulating response.

High-pressure infrared reflectivity spectra were acquired at the infrared beamline of the Swiss Light Source [26] using a diamond-anvil cell-based customized setup [27] fitting a Hyperion microscope. Freshly cut ~0.03 × 0.04 × 0.01-mm samples with the surface oriented parallel to the *c* and *b* axes were loaded in the sample chamber consisting of CuBe gaskets with ruby chips. We used KBr powder as a pressure transmitting medium. Since with this procedure the samples

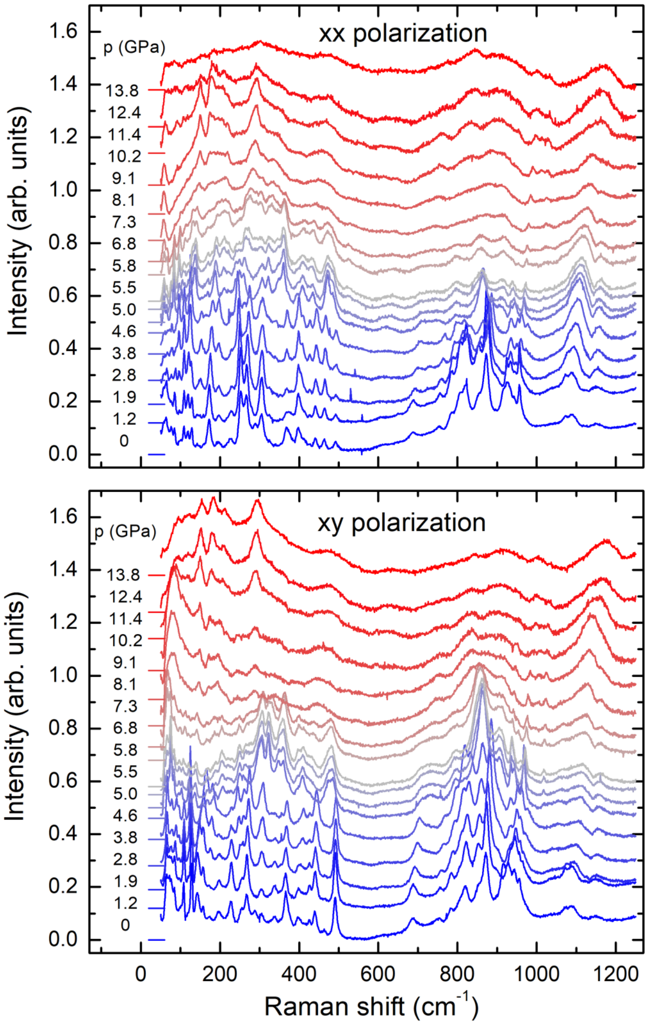

FIG. 4. Raman spectra for XX (top)and XY (bottom) polarizations. The curves have been given vertical offsets proportional to the applied pressure. The baseline for each pressure is indicated as a horizontal line on the left-hand side of the spectra, and pressures are indicated in the color coding of each spectrum.

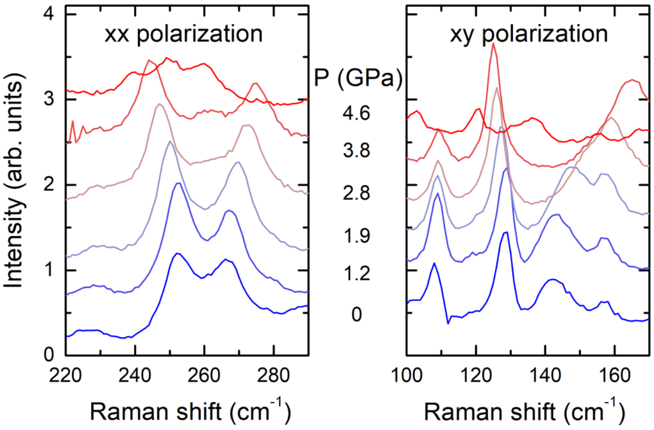

FIG. 5. Closeup of the Raman spectra for the (a) XX and (b) XY polarizations. The curves have been given vertical offsets in proportion to the applied pressure.

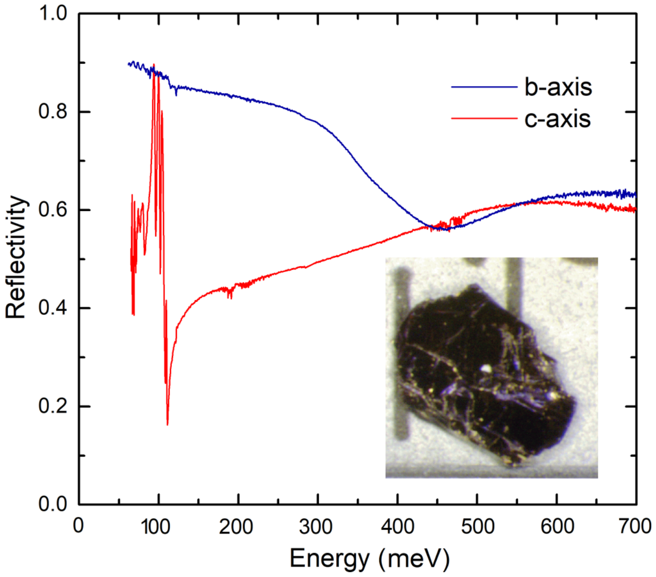

FIG. 6. Room-temperature reflectivity along the insulating and conducting axes at ambient pressure. The inset: One of the crystals used in the present paper.

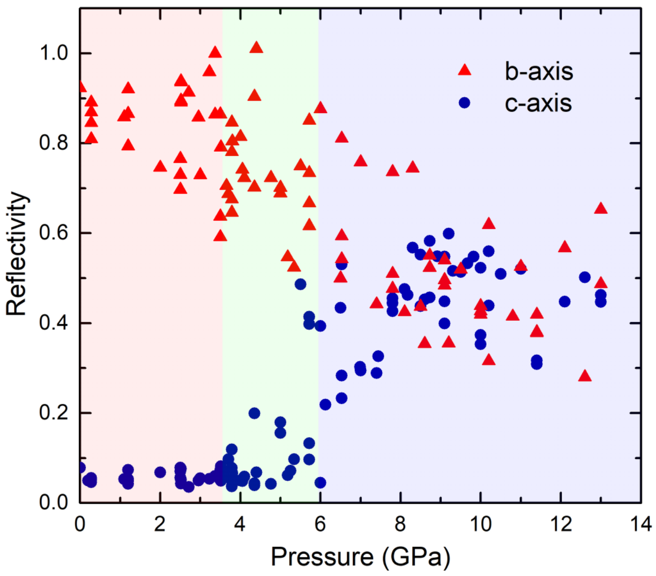

FIG. 7. Pressure dependence of the reflectivity at 124 meV ($1000\ \mathrm{cm}^{-1}$) for the *b* (red triangles) and *c* (blue dots) axes.

are pressed against the diamond window, the measured reflectivity spectra are those of a sample/diamond interface. A limited spectral range of 50–600 meV is imposed by the presence of a KBr window between the spectrometer and the microscope as well as the use of a gold wire far-infrared–mid-infrared polarizer located at the rear of the reflective objective. As the pressure is tuned at ambient temperature, a full thermal cycle is needed before changing the pressure inside the diamond-anvil cell. This together with the mechanical stabilization time reduce the number of accessible pressure points at low temperatures. To demonstrate the effect of pressure we begin with the reflectivity at 124 meV as a function of pressure, shown in Fig. 7 for light polarized both along the *b* and *c* axes. It should be mentioned at this point that due to the departure from 90° of the angle between *c* and *a*, the optical response of these two axes is, strictly speaking, not separated. The reflectivity polarized along *c* provides a pseudodielectric function of mixed *ac* character, and to correct for the mixing requires a combination of spectra on different crystal faces. In the present case the angle of 90.6° is sufficiently close to 90.0° to render these corrections too small to be relevant in the context of the present paper. The photon energy is selected such that it is higher than the observed phonon modes, and a large difference can be seen in *b* and *c* polarizations. The reflectivity along the initially more metallic *b* axis drops continuously. Consistent with the notion that metals make good mirrors due to the dielectric properties of free charge carriers, this drop of reflectivity indicates that the *b* axis becomes less conducting under pressure. On the other hand, the reflectivity along the initially insulating *c* axis becomes progressively higher above ∼4 GPa and finally reaches similar values as the *b*-axis reflectivity above 8 GPa. In principle, one should expect that the reflectivity progressively approaches the 100% level for $\omega \to 0$. Whether this behavior results from a transition toward a more conducting state along the *c* axis and a less conducting one along *b*, requires an analysis of the broad reflectivity spectra that we will now present.

The reflectivity spectra for selected pressures with the electric field polarized along the *c* axis and the *b* axis are displayed in Figs. 8 and 9, respectively. We calculated the optical conductivity $\sigma(\omega) = i\omega[1 - \epsilon(\omega)]/4\pi$ by fitting the reflectivity $R(\omega)$,

$$R(\omega) = \left| \frac{n_d - \sqrt{\epsilon(\omega)}}{n_d + \sqrt{\epsilon(\omega)}} \right|^2, \tag{1}$$

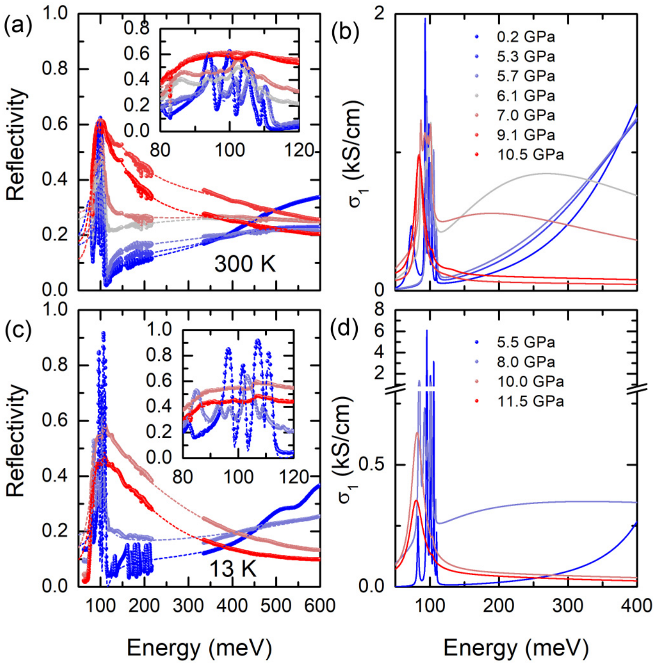

FIG. 8. Pressure-dependent evolution of the *c*-axis reflectivity and optical conductivity at room temperature and at 13 K.

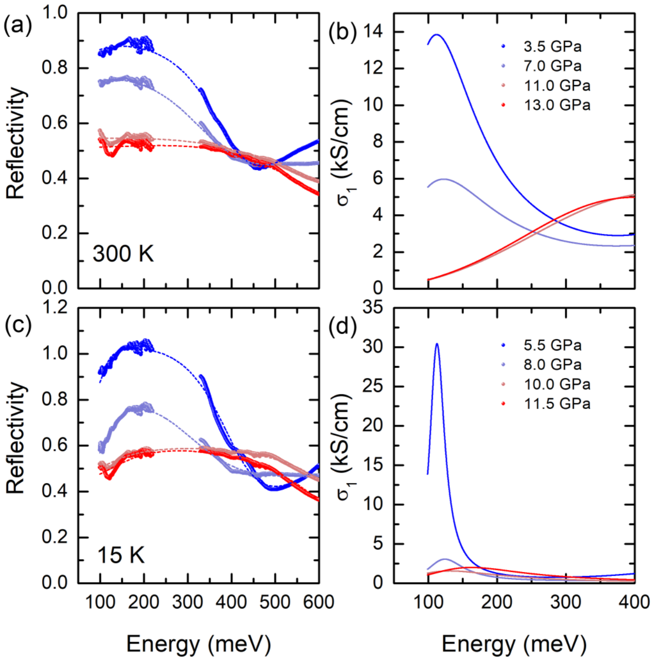

FIG. 9. Pressure-dependent evolution of the *b*-axis reflectivity and optical conductivity at 300 K and at 15 K.

where $n_d \approx 2.4$ is the optical constant of the diamond window to the Drude-Lorentz expansion,

$$\epsilon(\omega) = 1 - \sum_j \frac{\omega_{p,j}^2}{i\omega\gamma_j + \omega^2 - \omega_j^2}. \qquad (2)$$

At the lowest pressures, these data are qualitatively consistent with previous ambient pressure studies [17]. For all pressures from 0 up to 5.5 GPa the *c*-axis reflectivity shown in Fig. 8 is characteristic of an insulator with strong phonon modes and a low background level. At the highest pressures two phonon modes are evident, superimposed on a higher background. The main effect of cooling to 13 K [see Fig. 8, panels (a) and (c)] is a sharpening of the phonons and small shifts of the frequencies. From the optical conductivity shown in panels (b) and (d) we see that the intensities of the phonons do not change much as a function of pressure. More significant is the presence in the high-pressure phase of the continuum of excitations from the lower end of the measured frequency range (80 meV) and possibly lower to, at least, 200 meV or higher (note that due to optical absorption of the diamond, the reflectivity spectrum is cut between 200 and 300 eV). This continuum is clearly electronic in nature and could either be due to transitions across a small semiconductor gap (80 meV or smaller) or be due to intraband conductivity of strongly interacting electrons [28]. Either interpretation indicates a significant difference in the electronic properties along the *c* axis between low pressure [Figs. 1(a) and 1(c)] and high pressure [Figs. 1(b) and 1(d)], namely, a change from insulating behavior in the $P2_1/m$ phase to a small gap semiconductor or a bad metal in the $P2_1/a$ phase.

Contrary to the *c* axis, the reflectivity of the *b* axis displays no strong phononlike spectral features. At room temperature, the $\sigma_1(\omega)$ data seem to imply a gradual decrease in the Drude contribution. At low temperatures, the Drude contribution disappears entirely from our pressure and photon energy window. Under 5.5 GPa, a prominent feature appears—a narrow band at approximately 100 meV. The spectral weight exceeds typical phonon values by three orders of magnitude. The character of this band is, therefore, mainly electronic. We interpret this as a sideband of the Drude peak resulting from electron-phonon or electron-electron interactions [28].

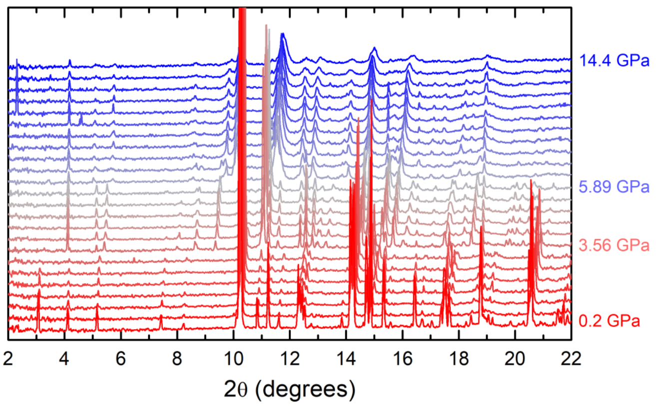

FIG. 10. Pressure ramp collected on powdered sample at BM 01, λ = 6.8043 Å, showing two phase transitions.

III. DISCUSSION

The x-ray diffraction, Raman, and infrared optical data reveal that as a function of pressure the system passes through a succession of different phases. These phases are summarized in Table I along with the crystallographic data obtained in the present paper.

Between ambient pressure and 3.0 GPa only the $P2_1/m$ phase is observed. The polyhedral drawing of the structure refined at 1.27 GPa is shown in Fig. 1. It appears that the buckling of corner-sharing octahedral chains in the ambient pressure phases increases upon pressure application (increase in the Mo-O-Mo angle between neighboring octahedra). Powder diffraction shows a structural transition most readily seen at scattering angles around $2\theta = 5.2^\circ$ and manifested by a pronounced peak splitting at 3.6 GPa (Figs. 2 and 10). In the ambient pressure phase, this intensity is composed of the 101 and $10\bar{1}$ Bragg reflections, which mark the monoclinic distortion and overlap entirely (within instrumental resolution) owed to the minor monoclinic angle of 90.66°. At the transition, this angle increases significantly to 93.5°, accompanied by a structural distortion and rearrangement of the coordination polyhedral, which is at the origin of the volume collapse (Fig. 2) of ~8% at this first transition. This rather large increase is surely triggered by the relative compliance of the coordination polyhedron formed around the Li atom [29].

Between 3.0 and 3.6 GPa $P2_1/m$ and $P2_1/a$ phases coexist as seen in the Rietveld plot at 3.6 GPa (see the Appendix). The phase transition in this pressure range strongly affects the Raman spectrum. In particular, two groups of modes, one between 100 and 200 cm^{-1} in *XY* polarization and the other between 900 and 900 cm^{-1} in both polarizations, are present below the critical pressure and disappear completely above

4 GPa (see Figs. 4 and 5). In the infrared reflectivity along the c axis (Fig. 8) additional phonon features appear for pressure in this range, and the overall appearance of the phonon spectrum changes. At 300 K the phonon spectrum becomes drastically rearranged between 0.2 and 6.1 GPa. At 13 K the rearrangement happens between 5.5 and 8 GPa, indicating that at low temperatures the structure is more resilient against pressure-induced changes than at 300 K. This change happens rather gradually, which is consistent with the coexistence of two phases.

Between 3.6 and 6.0 GPa (HP1) only the $P2_1/a$ phase is observed. This space group is confirmed by single-crystal diffraction data in the reciprocal-space reconstructions of the $0kl$, $1kl$, and $-1kl$ planes at 4.14 GPa (see the Appendix). The primitive cell of the $P2_1/a$ structure contains four formula units as compared to two formula units for the $P2_1/m$ structure at low pressures. Correspondingly, the c axis of the $P2_1/a$ structure is doubled as compared to $P2_1/m$. Lattice parameters obtained from LeBail fits to powder data are given in Table I. During this symmetry change, all Mo coordination centers move away from the special Wyckoff site $2e$ on the mirror plane at $y = 1/4$ in the ambient pressure phase ($P2_1/m$) to the lower symmetry general position $4e$ in the ($P2_1/a$) phase. At the transition pressure, one tetrahedral and one octahedral position merge into edge-sharing dimers, which form edge-sharing chains along the b axis in the $P2_1/a$ phase (light-green in Fig. 1). A strong buckling of the surrounding corner-sharing octahedral zigzag chains is observed. It is known that not only changes in connectivity as the present ones, but also changes in octahedral tilting affect the band dispersion within the band structure. The most significant structural change for the transport properties is the rearrangement of the MoO_4 tetrahedra and part of MoO_6 octahedra in the $P2_1/a$ phase due to which MoO_6 octahedra in adjacent slabs now share corners connecting the slabs along the a direction. The band structure of this new phase has not yet been reported. The aforementioned rearrangement of the MoO_4 tetrahedra, in particular, the corner sharing along a, increases the hopping between the slabs, and introduces hopping paths of MoO_6 octahedra along the c axis which are absent in the $P2_1/m$ phase. All in all this is expected to make the band dispersion in the $P2_1/a$ phase more three dimensional than in the $P2_1/m$ phase, which is qualitatively consistent with our optical data.

Above 6 GPa (HP2) a new crystallographic phase is formed (Fig. 2) whose primitive lattice, closely related to the one of the $P2_1/a$ phase, we were able to determine (see Table I) but whose atomic structure we could not solve. Lattice parameters were, nevertheless, refined from the powder-diffraction data with a LeBail fit. Indexation of the data (not high quality) no longer shows evidence of the superstructure in c. This structural transition appears to be triggering the dimensional crossover. Interestingly, an analysis of reciprocal-space reconstructions reveals a doubling of the b axis possibly due to a CDW (see the Appendix, weak intensities at $k = -1.5$) for which pressures we observe a gradual decrease in conductivity. For all pressures from 0 up to 5.5 GPa the c-axis optical reflectivity spectra (Fig. 8) display the characteristic features of optical phonons in the insulating state, whereas at higher pressures most phonon features disappear whereas the reflectivity rises with increasing pressure. The reflectivity spectrum above 5.5 GPa is characteristic of a metal with a fairly high value and weak phonon peaks where the dielectric function is dominated by the electronic screening. The pressure induces significant spectral changes in the b-axis optical conductivity (Fig. 9). Above 5.5 GPa the b-axis reflectivity strongly decreases, whereas the band in $\sigma_1(\omega)$ at 100 meV broadens, and its intensity gets suppressed at approximately 7 GPa. Taken together this behavior of the optical response is indicative of a loss of free-carrier spectral weight along the b axis in the high-pressure phase above 5.5 GPa.

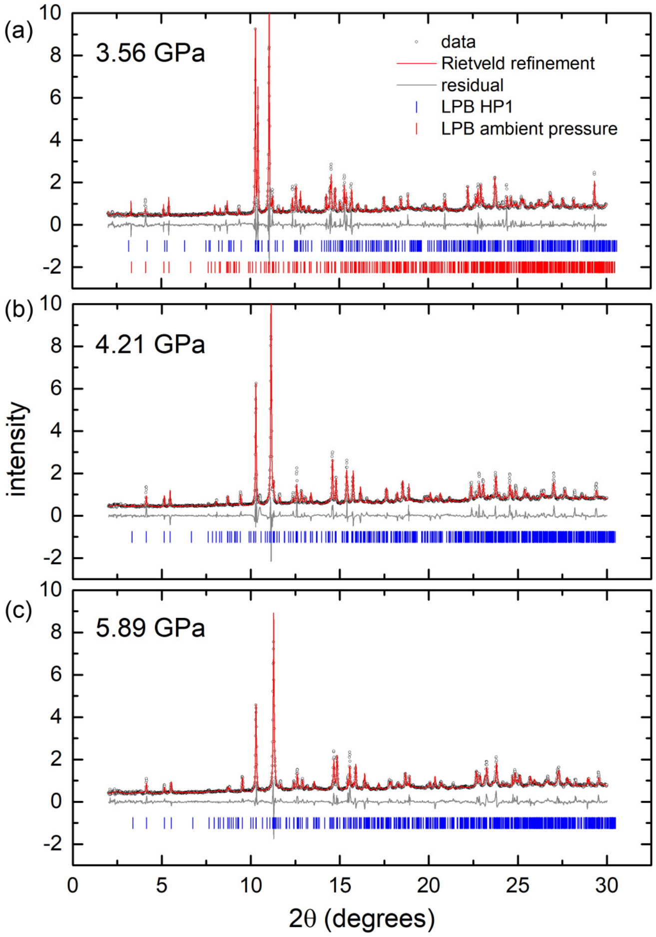

FIG. 11. Rietveld refinement at (a) 3.56 GPa, (b) 4.21 GPa, and (c) 5.89 GPa (bottom) with $\lambda = 0.680\,43$ Å. Symbols are $Li_{0.9}Mo_6O_{17}$ diffraction data, red curves are Rietveld refinement, and gray curves are fit residuals. The vertical line represents the positions of diffraction pictures of $Li_{0.9}Mo_6O_{17}$ in the ambient pressure structure (red) and in the high-pressure HP1 structure (blue).

The positive slope of the conductivity at 400 meV visible in Figs. 8 and 9 for pressures below 6 GPa gets suppressed at higher pressures. Instead, a broadband appears in the range below 400 meV. This is indicative of a rearrangement of the electronic bands. This has the effect that interband transitions seen along the b axis at 500 meV disappear, the material becomes a less good conductor along b, and the material becomes a better conductor along the c axis. All in all this implies that the phase above 5.5 GPa is electronically more isotropic with a metallic conductivity along the b and c axes.

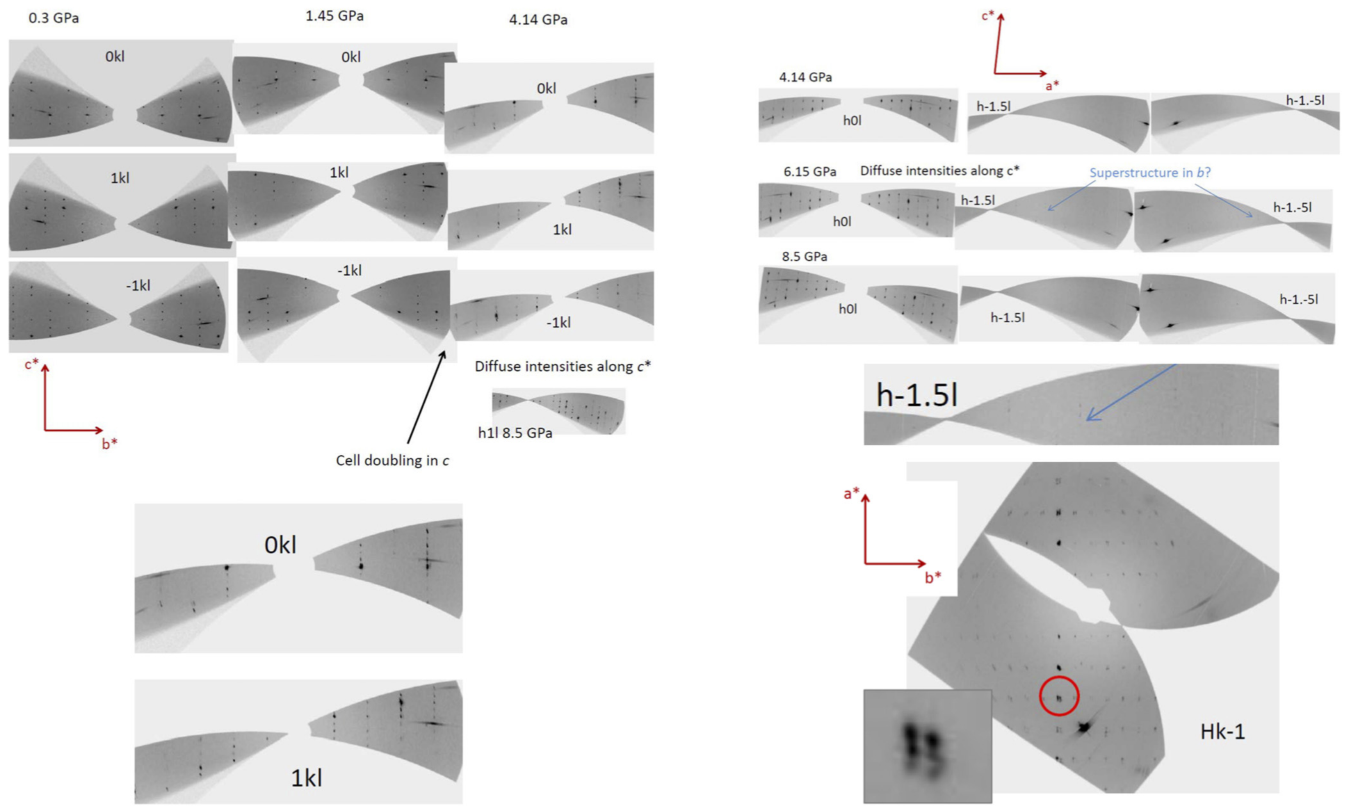

FIG. 12. Reciprocal-space reconstruction for different pressures. For all panels $\lambda = 0.3738$ Å. The data show cell doubling of c at 4.14 GPa, doubling of b at 6.15 GPa, and Bragg intensity splitting on the a-b plane at 8.5 GPa (lower right image).

8.5 GPa is the highest pressure for which single-crystal x-ray diffraction data could be collected. Here the $hk\bar{1}$ plane shows splitting of Bragg reflection related to structural changes on the ab plane (see the Appendix), which can, at present, not be investigated due to the lack of data quality. It should be noted that all structural changes observed up to the highest pressures are fully reversible on single-crystal samples, and refinements collected outside the diamond-anvil cell in previously pressurized crystal yield good R_1 values of approximately 3%, which are comparable to those collected prior to pressurization and demonstrate a very high reversible flexibility of the lattice. The Raman spectra above 9 GPa (Fig. 4) are characterized by a strong broadening and loss of intensity of the modes in XY polarization.

IV. CONCLUSIONS

The application of high pressure on $\mathrm{Li_{0.9}Mo_6O_{17}}$ strongly affects its crystal structure which remains in its ambient $P2_1/m$ phase up to near 3 GPa where it changes to the $P2_1/a$. This phase lasts up to 6 GPa. At 6 GPa a transition takes place to yet another monoclinic phase which is metallic both along b and c axes. This trend is observed at room temperature and at 13 K. This behavior is not surprising since pressure generally tends to increase the orbital overlap favoring increased mobility as observed in many quasi-1D organic compounds. An intriguing and counterintuitive aspect is the observation of a decreasing conductivity along the conducting axis. This apparent pressure-induced decrease in anisotropy is a clear indication that $\mathrm{Li_{0.9}Mo_6O_{17}}$ is driven away from its initial quasi-1D-dimensional conduction scenario.

The datasets generated and analyzed during the current paper are available in Ref. [11]. These will be preserved for 10 yr. All other data that support the plots within this paper and other findings of this paper are available from the corresponding author upon reasonable request.

ACKNOWLEDGMENTS

We thank T. Giamarchi and R. Černý for stimulating discussions. J.W.A. thanks O. K. Andersen for illuminating discussions of the two a-c axes labeling schemes in the literature. We are grateful to M. Brandt for technical assistance. This project was supported by the Swiss National Science Foundation through Projects No. 200020-135085, No. P00P2_170544, and No. 200020-179157. We are grateful for beam time allocation by the ESRF and the Swiss-Norwegian Beamlines (SNBL) and acknowledge local support from P. Parisiades from ID 27 and V. Dmitriev from SNBL.

APPENDIX: X-RAY DIFFRACTION

The powder-diffraction data were integrated to 1D diffraction patterns using FIT2D [30]. An example for different pressures is shown in Fig. 11. Direct-space modeling was performed in FOX [31], data were then refined with the Rietveld method using TOPAS5 [32]. During Rietveld refinement antibump restraints were applied to the Mo-Mo and Mo-O interatomic distances. No texture corrections were required, evidencing hydrostatic pressure conditions in the pressure chamber. We note that the Li position occupied to 90% was omitted from refinements as it was not visible by x-ray diffraction and/or its positional shifts did not behave in a stable way during minimization. This is not a surprise given the inherently lower quality of high-pressure diffraction data and the lack of contrast between the relatively light Li atom and its surroundings. Selected Rietveld refinements of the first high-pressure phase (3–6 GPa) are shown in Fig. 11.

Single-crystal data were treated with the SNBL tool [33] and CRYSALIS(PRO) [34] and refined using SHELXL [35] through the OLEX2 [36] user interface. Reciprocal-space reconstructions (Fig. 12) were performed with CRYSALIS(PRO). Single-crystal refinements were performed on BM 01 data only as the collected number of reflections was higher due to the larger opening angle of the diamond-anvil cell and the more favorable orientation of the loaded crystal. Data integration on the respective data sets yielded R_{int}'s of 3–3.5%, least-squares refinement resulted in R_1 values of 11 to 12%, which is acceptable for high-pressure experiments and a discussion of the general topology of the structure. The structure the phase between 3 and 6 GPa could not be solved directly from single-crystal data and was instead modeled by global optimization using FOX [31] on powder data obtained at 5.9 GPa. Despite the applied pressure, there is no evidence of preferred orientation, which supports the accuracy (at low resolution) of the model obtained by direct-space methods. This obtained minimized model was then used as an input model for Rietveld refinements as well as single-crystal structure refinements.

---

[1] M. Greenblatt, Molybdenum oxide bronzes with quasi-low-dimensional properties, Chem. Rev. **88**, 31 (1988).

[2] J. D. Denlinger, G. H. Gweon, J. W. Allen, C. G. Olson, J. Marcus, C. Schlenker, and L. S. Hsu, Non-Fermi-Liquid Single Particle Line Shape of the Quasi-One-Dimensional Non-CDW Metal $Li_{0.9}Mo_6O_{17}$: Comparison to the Luttinger Liquid, Phys. Rev. Lett. **82**, 2540 (1999).

[3] F. Wang, J. V. Alvarez, S. K. Mo, J. W. Allen, G. H. Gweon, J. He, R. Jin, D. Mandrus, and H. Höchst, New Luttinger-Liquid Physics from Photoemission on $Li_{0.9}Mo_6O_{17}$, Phys. Rev. Lett. **96**, 196403 (2006).

[4] M. Greenblatt, W. H. McCarroll, R. Neifeld, M. Croft, and J. V. Waszczak, Quasi two-dimensional electronic properties of the lithium molybdenum bronze, $Li_{0.9}Mo_6O_{17}$, Solid State Commun. **51**, 671 (1984).

[5] J. F. Mercure, A. F. Bangura, X. Xu, N. Wakeham, A. Carrington, P. Walmsley, M. Greenblatt, and N. E. Hussey, Upper Critical Magnetic Field far above the Paramagnetic Pair-Breaking Limit of Superconducting One-Dimensional $Li_{0.9}Mo_6O_{17}$ Single Crystals, Phys. Rev. Lett. **108**, 187003 (2012).

[6] L. Dudy, J. D. Denlinger, J. W. Allen, F. Wang, J. He, D. Hitchcock, A. Sekiyama, and S. Suga, Photoemission spectroscopy and the unusually robust one-dimensional physics of lithium purple bronze, J. Phys.: Condens. Matter **25**, 014007 (2012).

[7] L. Dudy, J. W. Allen, J. D. Denlinger, J. He, M. Greenblatt, M. W. Haverkort, Y. Nohara, and O. K. Andersen, ARPES and NMTO wannier orbital theory of $Li_{0.9}Mo_6O_{17}$ - implications for unusually robust quasi-one dimensional behavior, arXiv:1812.03388.

[8] G. Wu, X. Ye, X. Zeng, B. Wu, and W. G. Clark, Direct observation of charge state in the quasi-one-dimensional conductor $Li_{0.9}Mo_6O_{17}$, Sci. Rep. **6**, 20721 (2016).

[9] G. Wu, X. Ye, X. Zeng, B. Wu, and W. G. Clark, Investigation of the magnetic dipole field at the atomic scale in quasi-one-dimensional paramagnetic conductor $Li_{0.9}Mo_6O_{17}$, J. Phys.: Condens. Matter **28**, 015003 (2016).

[10] http://www.jp-minerals.org/vesta/en/.

[11] M. K. Tran, A. Akrap, J. Levallois, J. Teyssier, P. Schouwink, C. Besnard, P. Lerch, J. W. Allen, M. Greenblatt, and D. van der Marel, Open Data doi: 10.26037/yareta:oz4jlopcwnen5ndnsfpojaqjqa (2021).

[12] M. Onoda, K. Toriumi, Y. Matsuda, and M. Sato, Crystal structure of lithium molybdenum purple bronze $Li_{0.9}Mo_6O_{17}$, J. Solid State Chem. **66**, 163 (1987).

[13] D. Boies, C. Bourbonnais, and A. M. S. Tremblay, One-Particle and Two-Particle Instability of Coupled Luttinger Liquids, Phys. Rev. Lett. **74**, 968 (1995).

[14] T. Giamarchi, Viewpoint: Deconstructing the electron, Physics **2**, 78 (2009).

[15] J. Lu, X. Xu, M. Greenblatt, R. Jin, P. Tinnemans, S. Licciardello, M. R. van Delft, J. Buhot, P. Chudzinski, and N. E. Hussey, Emergence of a real-space symmetry axis in the magnetoresistance of the one-dimensional conductor $Li_{0.9}Mo_6O_{17}$, Sci. Adv. **5**, eaar8027 (2019).

[16] L. Degiorgi, P. Wachter, M. Greenblatt, W. H. McCarroll, K. V. Ramanujachary, J. Marcus, and C. Schlenker, Optical investigation of quasi-one- and two-dimensional systems $A_{0.9}Mo_6O_{17}$ (A=Li, K, and Na), Phys. Rev. B **38**, 5821 (1988).

[17] J. Choi, J. L. Musfeldt, J. He, R. Jin, J. R. Thompson, D. Mandrus, X. N. Lin, V. A. Bondarenko, and J. W. Brill, Probing localization effects in $Li_{0.9}Mo_6O_{17}$ purple bronze: An optical-properties investigation, Phys. Rev. B **69**, 085120 (2004).

[18] P. Chudzinski, T. Jarlborg, and T. Giamarchi, Luttinger-liquid theory of purple bronze $Li_{0.9}Mo_6O_{17}$ in the charge regime, Phys. Rev. B **86**, 075147 (2012).

[19] C. Escribe-Filippini, J. Beille, M. Boujida, J. Marcus, and C. Schlenker, Pressure effect on the transport properties of superconducting $Li_{0.9}Mo_6O_{17}$ bronze, Physica C **162–164**, 427 (1989).

[20] B. Sipos, A. F. Kusmartseva, A. Akrap, H. Berger, and L. Forro, From Mott state to superconductivity in 1T-TaS_2, Nature Mater. **7**, 960 (2008).

[21] C. Berthod, T. Giamarchi, S. Biermann, and A. Georges, Breakup of the Fermi Surface Near the Mott Transition in Low-Dimensional Systems, Phys. Rev. Lett. **97**, 136401 (2006).

[22] C. A. M. dos Santos, B. D. White, Y.-K. Yu, J. J. Neumeier, and J. A. Souza, Dimensional Crossover in the Purple Bronze $Li_{0.9}Mo_6O_{17}$, Phys. Rev. Lett. **98**, 266405 (2007).

[23] W. H. McCarroll and M. Greenblatt, Preparation of lithium molybdenum oxide bronzes by a temperature gradient flux growth technique, J. Solid State Chem. **54**, 282 (1984).

[24] B. Periotto, F. Nestola, T. Balic-Zunic, R. Angel, R. Miletich, and L. Olsen, Comparison between beryllium and diamond-backing plates in diamond-anvil cells: Application to single-crystal x-ray diffraction high-pressure data, Rev. Sci. Instrum. **82**, 055111 (2011).

[25] R. Miletich, D. R. Allan, and W. F. Kuhs, High-Pressure Single-Crystal Techniques, Rev. Mineral. Geochem. **41**, 445 (2000).

[26] P. Lerch, L. Quaroni, J. Wambach, J. Schneider, D. B. Armstrong, D. Rossetti, F. L. Mueller, P. Peier, V. Schlott, L. Carroll, P. Friedli, H. Sigg, S. Stutz, and M. Tran, IR beamline at the Swiss Light Source, J. Phys.: Conf. Ser. **359**, 012003 (2012).

[27] M. K. Tran, J. Levallois, A. Akrap, J. Teyssier, A. B. Kuzmenko, F. Lévy-Bertrand, R. Tediosi, M. Brandt, P. Lerch, and D. van der Marel, Versatile setup for optical spectroscopy under high pressure and low temperature, Rev. Sci. Instrum. **86**, 105102 (2015).

[28] D. N. Basov, R. D. Averitt, D. van der Marel, M. Dressel, and K. Haule, Electrodynamics of correlated electron materials, Rev. Mod. Phys. **83**, 471 (2011).

[29] Li is omitted from the structural drawings as it could be located neither from powder nor from single-crystal diffraction under pressure.

[30] A. P. Hammersley, S. O. Svensson, and A. Thompson, Calibration and correction of spatial distortions in 2D detector systems, Nucl. Instrum. Methods Phys. Res., Sect. A Detectors and Associated Equipment **346**, 312 (1994).

[31] R. Černý and V. Favre-Nicolin, Direct space methods of structure determination from powder diffraction: Principles, guidelines and perspectives, Z. Kristallogr. **222**, 105 (2007).

[32] A. A. Coelho, TOPAS and TOPAS-Academic: An optimization program integrating computer algebra and crystallographic objects written in C + +, J. Appl. Cryst. **51**, 210 (2018).

[33] V. Dyadkin, P. Pattison, V. Dmitriev, and D. Chernyshov, A new multipurpose diffractometer PILATUS@SNBL, J. Synchrotron Rad. **23**, 825 (2016).

[34] Oxford Diffraction Agilent Technologies UK Ltd, CrysAlisPRO User Manual (Agilent, Oxfordshire, U.K., 2013).

[35] G. M. Sheldrick, Crystal structure refinement with SHELXL, Acta Cryst. **C 71**, 3 (2015).

[36] O. V. Dolomanov, L. J. Bourhis, R. J. Gildea, J. A. K. Howard, and H. Puschmann, OLEX2: A complete structure solution, refinement and analysis program, J. Appl. Crystallogr. **42**, 339 (2009).